Thin Ice DEM Model Based on Smoothed Elements: A 2.5-Dimensional DEM Approach for Ice–Structure Interaction Simulation

Oleg Konovalov[1], Lu Liu[2], Shunying Ji[2]

[1]Belarusian State University, Department of Applied Mathematics, Minsk, Belarus
[2]Dalian University of Technology, State Key Laboratory of Structural Analysis for Industrial Equipment, Dalian, China

Corresponding author: Oleg Konovalov
Email: `konovalovol@bsu.by`

ORCID: https://orcid.org/0009-0009-6367-4655

Keywords: discrete element method, thin ice, reduced degrees of freedom, ice–structure interaction, RMIB, Voronoi tessellation, shallow water, GPU computing

Abstract: We present a novel 2.5-dimensional Discrete Element Method (DEM) model, termed the Thin Ice Model (TIM), for efficient simulation of ice–structure interactions in broken and unbroken sea ice fields. The model is based on Voronoi tessellation of a single-layer ice sheet, where the ratio of element area to thickness exceeds 10. By constraining the degrees of freedom from six (full 3D) to four—retaining only yaw rotation—the model ensures that all computational cells remain horizontal, enabling contact force calculations via 2D convex polygon intersection rather than costly 3D intersection algorithms. This simplification reduces the computational cost compared to full 3D DEM formulations and is naturally suited for parallel implementation, including GPU–CUDA architectures. A modified Real Multidimensional Internal Bond (RMIB) approach is employed to model intact ice sheet failure, with an original separation of normal forces into horizontal and vertical components, controlled by smoothing functions $K(z)$. The model is validated against model-scale shallow-water ice–structure interaction experiments by Lemström and Polojärvi (2022) for weak, medium, and strong ice. The structural contact stiffness in the simulation is matched to the effective stiffness of the composite experimental panel, requiring no ice-type-specific fitting. The steady-state horizontal ice load is reproduced with errors below 1% for weak and medium ice and 18% for strong ice, the latter attributed to the simulation not having fully reached the steady-state phase. The peak load for strong ice matches the experiment within 2%. The model correctly captures the experimentally observed non-proportionality of ice load and ice strength, whereby weak ice yields a higher steady-state load than medium ice. Rubble pile geometries are reproduced for the strong ice case.

Thin Ice DEM Model Based on Smoothed Elements: A 2.5-Dimensional DEM Approach for Ice–Structure Interaction Simulation

Oleg Konovalov* Lu Liu† Shunying Ji‡

2025

Abstract

We present a novel 2.5-dimensional Discrete Element Method (DEM) model, termed the Thin Ice Model (TIM), for efficient simulation of ice–structure interactions in broken and unbroken sea ice fields. The model is based on Voronoi tessellation of a single-layer ice sheet, where the ratio of element area to thickness exceeds 10. By constraining the degrees of freedom from six (full 3D) to four—retaining only yaw rotation—the model ensures that all computational cells remain horizontal, enabling contact force calculations via 2D convex polygon intersection rather than costly 3D intersection algorithms. This simplification reduces the computational cost compared to full 3D DEM formulations and is naturally suited for parallel implementation, including GPU–CUDA architectures. A modified Real Multidimensional Internal Bond (RMIB) approach is employed to model intact ice sheet failure, with an original separation of normal forces into horizontal and vertical components, controlled by smoothing functions $K(z)$. The model is validated against model-scale shallow-water ice–structure interaction experiments by Lemström and Polojärvi (2022) for weak, medium, and strong ice. The structural contact stiffness in the simulation is matched to the effective stiffness of the composite experimental panel, requiring no ice-type-specific fitting. The steady-state horizontal ice load is reproduced with errors below 1% for weak and medium ice and 18% for strong ice, the latter attributed to the simulation not having fully reached the steady-state phase. The peak load for strong ice matches the experiment within 2%. The model correctly captures the experimentally observed non-proportionality of ice load and ice strength, whereby weak ice yields a higher steady-state load than medium ice. Rubble pile geometries are reproduced for the strong ice case.

Keywords: discrete element method, thin ice, reduced degrees of freedom, ice–structure interaction, RMIB, Voronoi tessellation, shallow water, GPU computing

1 Introduction

Simulations of ice–structure interaction require consideration of a complex process including fragmentation of intact ice fields, formation and motion of ice blocks, interactions between the blocks, and interactions between the blocks and the structure. Due to the discrete nature of broken ice, the Discrete Element Method (DEM) plays a central role in the development of numerical simulation programs for both broken and unbroken ice conditions [1, 2].

For simulations of intact ice sheet and its failure, combined finite–discrete element methods have been proposed, including lattices of Timoshenko beams [3] and bonded discrete element

*Belarusian State University, Department of Applied Mathematics, Minsk, Belarus

†Dalian University of Technology, State Key Laboratory of Structural Analysis for Industrial Equipment, Dalian, China

‡Dalian University of Technology, State Key Laboratory of Structural Analysis for Industrial Equipment, Dalian, China

methods [4, 5]. However, full 3D DEM+FEM formulations are computationally very demanding in terms of both time and equipment. As noted by many authors in the field of engineering-scale ice mechanics, the question arises: "3D modeling is computationally very challenging compared to 2D simulation—is there a need for 3D modeling?"

Several GPU-accelerated DEM approaches for ice simulation have been proposed in recent years. Daley et al. [7] and Alawneh et al. [8] developed GPGPU-based models for ship operations in pack ice, achieving near-real-time performance. Liu and Ji [9] implemented a GPU-based DEM for ice resistance on ship hulls in level ice. Full 3D DEM formulations have been applied to pressure ridge formation [11] and regional-scale sea ice drift [12]. Real-time ship–ice interaction models have also been developed by Lubbad and Løset [13], building on energy-based ice collision force formulations [14]. The TIM model presented here differs from these approaches by reducing the DOF from 6 to 4 and employing a 2D contact model, which avoids the 3D tolerance problems inherent in GPU implementations of full 3D DEM.

While certain phenomena cannot be modeled using 2D approaches, we pose the question: *is there an intermediate approach between 2D and 3D?* In this work, we propose a 2.5-dimensional approach—the Thin Ice Model (TIM)—and develop a numerically efficient algorithm that is more efficient than full 3D DEM, with efficiency achieved through reduced degrees of freedom and simplified contact detection. A GPU–CUDA implementation of the model is described in Section 3, and a detailed quantitative performance analysis is deferred to a follow-up study.

The remainder of this paper is organized as follows. Section 2 describes the TIM formulation, including element geometry, kinematic constraints, contact mechanics, smoothing functions, and the RMIB bond model. Section 3 details the implementation, including the CUDA-based computational cycle. Section 4 presents the validation against model-scale experiments. Section 5 discusses the results, and Section 6 draws conclusions.

2 Thin Ice DEM Model

2.1 Element Geometry

The TIM is a single-layer ice model based on Voronoi tessellation, where the ratio of the element area to its thickness is greater than 10 (Fig. 1). Each element represents a thin ice fragment characterized by its in-plane polygonal shape and uniform thickness h.

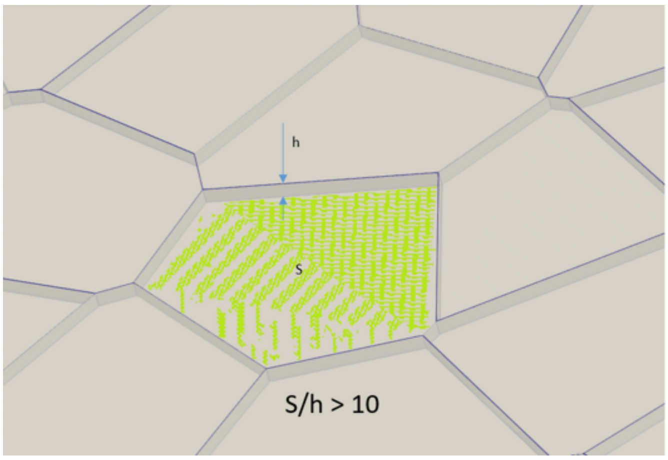

Figure 1: Single-layer ice model based on Voronoi tessellation. The ratio of element area to thickness is greater than 10.

2.2 Constraints of Degrees of Freedom

In the classical 3D DEM formulation, each particle has six degrees of freedom: three translational and three rotational. In the TIM, we decrease the number of degrees of freedom from six to four by retaining only:

- Three translational degrees of freedom (x, y, z);
- Only **yaw rotation** (rotation about the Z axis).

The roll and pitch rotations are constrained. As a result, the cells in the TIM are *always horizontal* (Fig. 2).

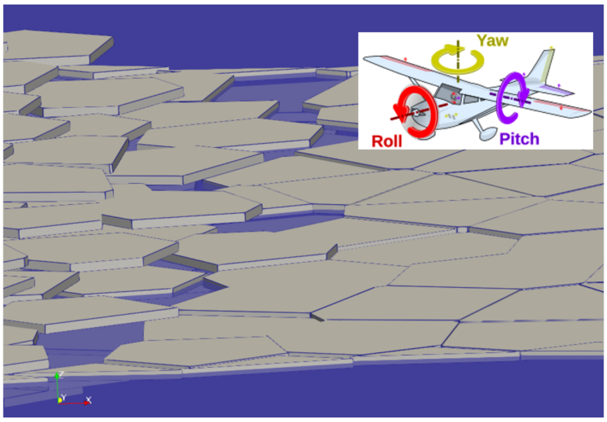

Figure 2: Constraints of degrees of freedom in TIM. Only yaw rotation (about the Z axis) is retained, reducing DOF from 6 to 4. All cells remain horizontal.

This constraint is the foundation of the model's computational efficiency, as it enables:

1. Contact force calculations based on 2D convex polygon intersection;
2. Contact detection using a plane KD-tree with nearest-neighbor queries of fixed radius;
3. Simplified parallel implementation, including on GPU architectures, without 3D tolerance problems.

2.3 Dynamic Contact Model

In the classical 3D DEM, ice blocks are rigid or deformable 3D particles, and contact forces require calculation of 3D intersections for all connected particles. Accounting for tolerance problems, such algorithms are inefficient in parallel implementations, including GPU–CUDA architectures.

The yaw constraint of the TIM model enables contact forces based on **convex polygon intersection**, which is numerically much simpler and more tolerant (Fig. 3).

The contact forces are derived from two complementary models: a *planar* (2D) contact formulation for the horizontal force and a *one-dimensional* contact spring for the vertical force. This decomposition is a direct consequence of the TIM kinematic constraint—since all cells remain horizontal, the horizontal and vertical contact mechanics can be separated and computed independently.

Horizontal force: planar contact through intersection area. The horizontal (normal) force arises from the elastic interaction between two Voronoi cells whose 2D polygonal projections overlap in the horizontal (xy) plane. The contact zone is characterized by the intersection area S_{ij} of the two polygons. In the framework of plane-stress elasticity, the contact pressure

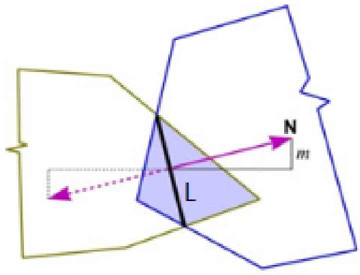

Figure 3: Dynamic contact model. The yaw constraint enables contact forces based on 2D convex polygon intersection. Formulas for normal force F_{ij}^n, vertical force F_{ij}^v, and moment M_{ij}^n are shown.

between two flat elastic bodies is proportional to the plane-stress modulus $E/(1-\nu)$ [15]. For the polygon-on-polygon geometry inherent to Voronoi tessellation, the contact stiffness additionally depends on the shape of the intersection zone, captured by the characteristic contact length L_{ij}. The factor 3 in the numerator accounts for the specific stiffness of a flat punch on an elastic half-space under plane-stress conditions.

The geometric ratio $S_{ij}/(h \cdot L_{ij})$ represents a dimensionless *contact strain*: the intersection area S_{ij} is normalized by the reference area $h \cdot L_{ij}$, where h is the ice thickness and L_{ij} is the characteristic length of the contact line between the two polygons. The additional factor $1/h$ converts this strain into a strain per unit thickness, yielding the full geometric factor $S_{ij}/(h^2 \cdot L_{ij})$.

The **horizontal (normal) force** between elements i and j:

$$F_{ij}^n = K_n\left(\frac{z_j - z_i}{h}\right) \cdot N_{ij} \cdot \frac{3E}{1-\nu} \cdot \frac{S_{ij}}{h^2 \cdot L_{ij}} \tag{1}$$

Vertical force: one-dimensional contact spring along Z. The vertical force is computed as a 1D elastic contact between the two cells along the vertical (Z) axis. When two cells at different vertical levels z_i and z_j have overlapping vertical projections, the quantity Z represents the *vertical overlap* (penetration depth) between the two cells:

$$Z = \max\left(0,\ h - |z_j - z_i|\right) \tag{2}$$

where h is the ice thickness. If the vertical offset exceeds the ice thickness ($|z_j - z_i| > h$), the cells are fully separated in the vertical direction and $Z = 0$.

The effective contact width perpendicular to the Z axis is given by S_{ij}/h, where S_{ij} is the horizontal intersection area distributed over the ice thickness. The vertical stiffness is then governed by the vertical Young's modulus E_v and Poisson's ratio ν through the factor $3E_v/(1-\nu)$, analogous to the plane-stress modulus but applied in the vertical direction. The full vertical force is:

$$F_{ij}^v = K_v\left(\frac{z_j - z_i}{h}\right) \cdot Z \cdot \frac{3E_v}{1-\nu} \cdot \frac{S_{ij}}{h} \tag{3}$$

The **moment**:

$$M_{ij}^n = F_{ij}^n \cdot m_{ij} \tag{4}$$

where the variables are defined as follows:

- $K_n(\frac{z_j - z_i}{h})$ and $K_v(\frac{z_j - z_i}{h})$ are the horizontal and vertical smoothing functions (Section 2.4), dimensionless, controlling the degradation of bond strength with vertical offset;
- $z_j - z_i$ is the vertical offset between the centroids of elements i and j [m];

- h is the ice thickness [m];
- N_{ij} is the contact normal—the unit vector in the horizontal (xy) plane perpendicular to the contact line between the overlapping polygon edges of elements i and j, directed from i to j [dimensionless];
- E and E_v are the horizontal and vertical Young's moduli of the ice [Pa]. For isotropic ice, $E = E_v$; for anisotropic or columnar ice, E_v may differ from E to reflect the directional dependence of elastic properties through the ice thickness;
- ν is Poisson's ratio [dimensionless];
- S_{ij} is the intersection area of the 2D polygonal projections of elements i and j onto the horizontal plane [m^2];
- L_{ij} is the characteristic contact length—a representative linear dimension of the intersection zone, typically taken as the length of the contact line or the square root of the intersection area [m];
- Z is the vertical overlap (penetration depth) between elements i and j along the Z axis, defined by Eq. (2) [m];
- m_{ij} is the moment arm—the perpendicular distance from the centroid of element i to the line of action of the horizontal contact force F_{ij}^n, determined by the geometry of the polygon intersection and the relative positions of the cell centroids [m].

The horizontal force F_{ij}^n (1) is a planar contact force: it is proportional to the intersection area S_{ij} (larger overlap produces stronger force), scaled by the plane-stress elastic modulus $3E/(1-\nu)$, and normalized by the geometric reference $h^2 \cdot L_{ij}$. The vertical force F_{ij}^v (3) is a 1D contact spring along Z: it is proportional to the vertical penetration Z (analogous to the overlap in classical DEM), with effective stiffness $K_v \cdot \frac{3E_v}{1-\nu} \cdot \frac{S_{ij}}{h}$. Both forces are modulated by their respective smoothing functions, which reduce the bond strength as the vertical offset between cells increases.

2.4 Smoothing Functions

Smoothing functions $K(z)$ are designed for the correction of connection forces for Voronoi cells placed at different vertical levels. The border values are:

$$K(0) = 1, \qquad K(z > 1) = 0 \tag{5}$$

These functions serve as an additional handle for constructing different ice properties (Fig. 4). For example, by selecting different smoothing functions, one can model weak or strong ice.

In this work, we employ a one-parameter family of smoothing functions defined as:

$$K_n(z) = (1-z)^n \cdot \Theta(1-z), \qquad z = \frac{|z_j - z_i|}{h} \tag{6}$$

where z is the vertical offset normalized by the ice thickness h, Θ is the Heaviside step function enforcing the compact support on $[0, 1]$, and n is the **smoothing exponent** that controls the rate of bond degradation with vertical displacement.

Three values of n are used to model the three ice types in the validation tests (Table 1):

The physical interpretation of the exponent n is as follows. The derivative of the smoothing function,

$$K_n'(z) = -n\,(1-z)^{n-1}, \tag{7}$$

Table 1: Smoothing exponent n for different ice types.

Ice type	n	$K_n(z)$
Weak (W)	2	$(1-z)^2$
Medium (M)	1	$(1-z)$
Strong (S)	1/2	$\sqrt{1-z}$

characterizes the sensitivity of the bond force to vertical displacement. A larger n implies a steeper initial decay of K_n near $z = 0$, meaning that even small vertical offsets between ice fragments rapidly weaken their bonds. This corresponds to brittle ice failure, where crack propagation dominates. Conversely, a smaller n produces a gentle initial decay with bonds remaining effective even at substantial vertical offsets, corresponding to a more ductile, viscoelastic failure mode.

Table 2 compares the values of $K_n(z)$ at representative offsets.

Table 2: Values of $K_n(z)$ at representative normalized vertical offsets.

n	$z=0$	$z=0.25$	$z=0.5$	$z=0.75$	$z=1$
1/2	1.000	0.866	0.707	0.500	0
1	1.000	0.750	0.500	0.250	0
2	1.000	0.563	0.250	0.063	0

For strong ice ($n = 1/2$), the bond retains 71% of its strength at a vertical offset of half the ice thickness ($z = 0.5$), whereas for weak ice ($n = 2$) the same offset reduces the bond to only 25% of its strength. This difference directly controls the fragmentation pattern: strong ice tends to fail in narrow, concentrated zones, while weak ice fragments more diffusely over a larger area.

The smoothing exponent n thus acts as a single material parameter bridging the continuum-scale ice properties (flexural strength, elastic modulus) and the discrete bond-level behavior in the RMIB framework.

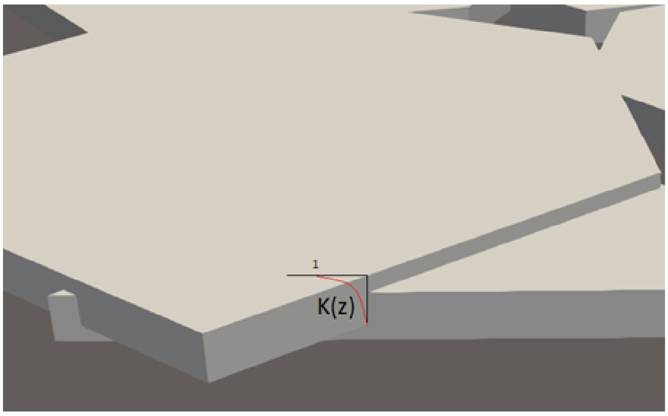

Figure 4: Smoothing functions $K(z)$ for correction of connection forces between Voronoi cells at different vertical levels. Border values: $K(0) = 1$, $K(z > 1) = 0$. Different functions model weak or strong ice.

2.5 Dynamic Contact Detection

The TIM assumption enables contact detection based on a **plane KD-tree** using nearest-neighbor requests with a fixed radius (Fig. 5). This 2D spatial data structure is significantly more efficient than 3D alternatives and is well-suited for parallelization, including on GPU architectures.

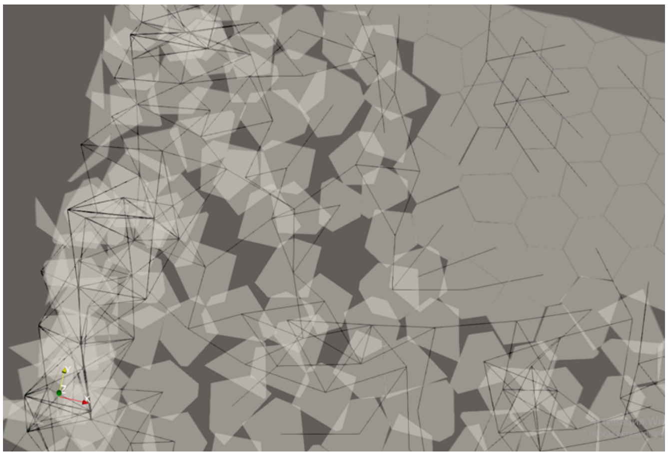

Figure 5: Dynamic contact detection using a plane KD-tree with nearest-neighbor queries of fixed radius, enabled by the TIM yaw constraint.

2.6 RMIB Bond Model for Intact Ice Failure

Classical DEM formulation is insufficient to describe the complicated process of intact ice sheet failure. Several authors have proposed models based on combined finite–discrete element methods, including:

- Lattice of Timoshenko beams [3];
- Bonded Discrete Element Method [4, 5];
- Bonded-particle sea ice model DESIgn [10].

In the TIM, we adopt the **Real Multidimensional Internal Bond (RMIB)** approach, which provides proper results for the failure of continuous geo-strata and is particularly amenable to parallel implementation due to its very simple computational kernel.

2.6.1 Interactions Between Particles

Let $\mathbf{n}_{ij}$ be the normal unit vector pointing from particle i to particle j (Fig. 6). The vector of relative displacement is:

$$\Delta\mathbf{u}_{ij} = \mathbf{u}_j - \mathbf{u}_i \tag{8}$$

The normal displacement:

$$\Delta\mathbf{u}_{ij}^n = (\Delta\mathbf{u}_{ij} \cdot \mathbf{n}_{ij})\,\mathbf{n}_{ij} \tag{9}$$

The simplified shear displacement:

$$\Delta\mathbf{u}_{ij}^s = \Delta\mathbf{u}_{ij} - \Delta\mathbf{u}_{ij}^n \tag{10}$$

The normal and shear forces:

$$F_{ij}^n = k_n \cdot |\Delta\mathbf{u}_{ij}^n|, \qquad F_{ij}^s = k_s \cdot |\Delta\mathbf{u}_{ij}^s| \tag{11}$$

where k_n and k_s are the stiffnesses of the normal and shear springs.

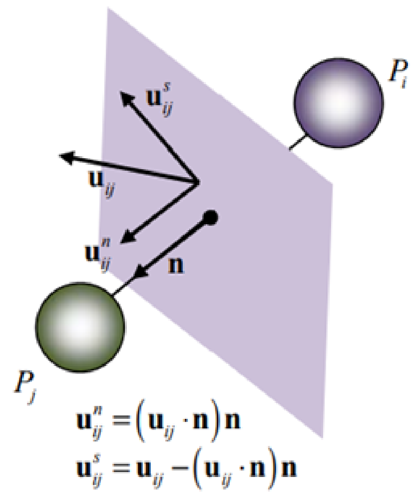

Figure 6: RMIB interactions between particles: (a) normal unit vector $\mathbf{n}_{ij}$, (b) relative displacement decomposition, (c) separation of normal force into horizontal F_{ij}^h and vertical F_{ij}^v components.

2.6.2 Modified RMIB: Separation of Horizontal and Vertical Forces

Our modification of the standard RMIB is the separation of F_{ij}^n into **horizontal** and **vertical** parts:

$$F_{ij}^n \longrightarrow F_{ij}^h + F_{ij}^v \tag{12}$$

This separation, combined with the smoothing functions $K(z)$, allows independent control of horizontal and vertical ice behavior.

2.6.3 Failure Criterion

Failure can only occur at the bond between particles (Fig. 7). The bond is broken when its horizontal or vertical stress exceeds the corresponding threshold:

$$\sigma_v > \sigma_f - \sigma_{\text{comp}} \cdot k \qquad \text{or} \qquad \sigma_h > \sigma_f \tag{13}$$

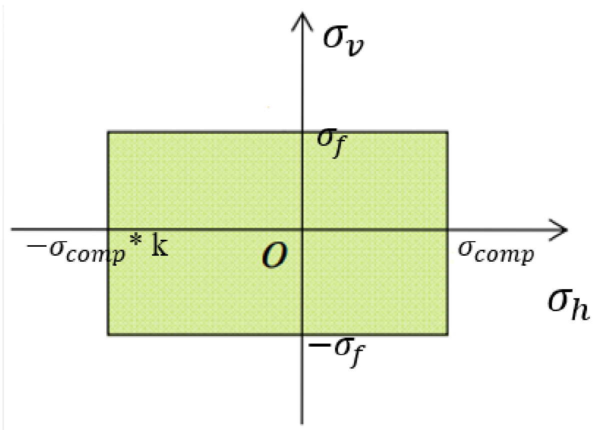

Figure 7: Failure criterion of the RMIB bond model. The bond breaks when vertical stress σ_v or horizontal stress σ_h exceeds the corresponding ultimate value (flexural strength σ_f or compressive strength σ_{comp}).

where:

- σ_v and σ_h are the vertical and horizontal stresses in the bond [Pa], computed from the corresponding bond forces F_{ij}^v and F_{ij}^n divided by the effective bond cross-sectional area;
- σ_f is the flexural (tensile) strength of the ice [Pa];
- σ_{comp} is the compressive strength of the ice [Pa];
- k is the **compression–failure coupling coefficient** [dimensionless], a model parameter that quantifies the influence of compressive stress on the vertical (flexural) failure threshold.

Interpretation of k. The vertical failure criterion in Eq. (13) states that the bond fails vertically when the vertical stress σ_v exceeds the flexural strength σ_f *reduced* by the compressive stress contribution $\sigma_{\mathrm{comp}} \cdot k$. The parameter k controls how much the compressive loading suppresses the vertical failure threshold:

- $k = 0$: compressive stress has no effect on flexural failure; the threshold is simply σ_f;
- $k > 0$: compressive stress *lowers* the vertical failure threshold, meaning that ice under compression becomes more susceptible to flexural (vertical) cracking. This captures the well-known observation in ice mechanics that compressive loading promotes vertical splitting and buckling-like failure modes [16];
- $k \approx \sigma_f/\sigma_{\mathrm{comp}}$: the vertical failure threshold approaches zero when the compressive stress reaches the compressive strength, meaning that the ice cannot sustain any additional flexural load at the point of compressive failure.

The horizontal failure criterion $\sigma_h > \sigma_f$ does not include a compression correction, reflecting the assumption that compressive loading primarily affects the vertical (out-of-plane) failure mode in thin ice.

The coefficient k requires calibration against experimental data for each ice type. In the present validation (Section 4), k is calibrated together with the smoothing exponent n (Section 2.4) to reproduce the measured horizontal ice loads for weak, medium, and strong ice.

2.7 Equations of Motion

The particle velocity is calculated individually as:

$$\mathbf{v}_i^{t+\Delta t} = \mathbf{v}_i^t + \frac{\mathbf{F}_i}{m_i}\,\Delta t \tag{14}$$

The new displacement:

$$\mathbf{u}_i^{t+\Delta t} = \mathbf{u}_i^t + \mathbf{v}_i^{t+\Delta t}\,\Delta t \tag{15}$$

The system of equations for the network of particles and bonds:

$$[M]\,\ddot{\mathbf{u}} + [C]\,\dot{\mathbf{u}} + [K]\,\mathbf{u} = \mathbf{F}(t) \tag{16}$$

where $\mathbf{u}$ is the particle displacement vector, $[K]$ is the stiffness matrix, $[M]$ is the diagonal mass matrix, $[C]$ is the damping matrix, and $\mathbf{F}(t)$ is the external force vector.

3 Implementation

The computational efficiency of the TIM model arises from two sources: the reduction of DOF from 6 to 4, and the use of 2D polygon intersection instead of 3D intersection algorithms. The model has been implemented with GPU–CUDA acceleration; this section describes the computational cycle and key implementation details. A detailed quantitative performance analysis (wall-clock time, memory consumption, and GPU/CPU speedup) is beyond the scope of this paper and will be presented in a follow-up publication.

The calculation cycle is organized as follows:

Algorithm 1 TIM calculation cycle

```
t ← 0
while t < t_max do
    kd_tree_dynamic_bond_calculation()            ▷ Build KD-tree, detect dynamic bonds
    move_model_to_gpu()                           ▷ Transfer data to GPU
    for iter = 1 to N_iter do                     ▷ Fixed inner iterations (e.g. N_iter = 1000)
        calculate_cells_and_structure_interaction()   ▷ Gravity, buoyancy, moments
        calculate_RMIB_static_bond_forces()
        calculate_RMIB_dynamic_bond_forces()
        calculate_DEM_dynamic_bond_forces()
        calculate_movement_velocity()
        calculate_rotation_velocity()
        update_particle_displacement()
        update_particle_rotation()
        Δ_disp ← max_displacement()
        Δ_rot ← max_rotation()
        if Δ_disp > 0.1 l̄ or Δ_rot > δ_rot then   ▷ l̄: mean Voronoi edge; δ_rot ≈ 1–5°
            break                                 ▷ Rebuild contacts
        end if
    end for
    move_from_gpu()
    t ← t + N_iter · Δt
end while
print_result()
```

The inner loop runs for a fixed number of iterations N_{iter} (typically 1000), during which all forces are computed and particle positions are updated on the GPU. After each inner iteration, the maximum displacement of particle centers Δ_{disp} and the maximum yaw rotation Δ_{rot} are evaluated. If either exceeds its threshold—$\Delta_{\text{disp}} > 0.1\,\bar{l}$, where $\bar{l}$ is the mean Voronoi cell edge length, or $\Delta_{\text{rot}} > \delta_{\text{rot}}$ with $\delta_{\text{rot}} \approx 1$–$5°$—the inner loop terminates prematurely and the KD-tree is rebuilt to update the dynamic contact network. This ensures that the contact detection remains accurate as particles move, while minimizing the computationally expensive KD-tree reconstruction on the CPU.

The implementation separates CPU and GPU responsibilities:

- **CPU**: KD-tree construction, dynamic bond calculation, data transfer management;
- **GPU**: All force calculations, velocity/displacement updates, convergence check.

Polygon intersection kernel. The contact area S_{ij} between two Voronoi cells is computed using a CUDA kernel implementing convex polygon intersection in integer arithmetic. The kernel scales the polygon coordinates to a large integer range (5×10^8) to avoid floating-point tolerance issues inherent in GPU arithmetic. A bounding-box pre-check eliminates non-intersecting edge pairs before the oriented-area tests, and the intersection area is accumulated using the shoelace formula. The kernel handles polygons with up to 10 intersection points, sufficient for typical Voronoi cells with 4–8 edges. This integer-based approach is one of the key advantages of the TIM yaw constraint: by keeping all cells horizontal, the 3D intersection problem is reduced to a well-conditioned 2D integer computation, eliminating the tolerance problems that plague 3D DEM implementations on GPU architectures.

The RMIB computational kernel is intentionally simple, making it well-suited for massive parallelization on CUDA cores.

3.1 Computational Advantages

The reduction of DOF from 6 to 4 and the use of 2D polygon intersection instead of 3D intersection algorithms provide two levels of computational advantage: fewer state variables per element and a simpler contact detection kernel. Table 3 summarizes the key differences between the TIM implementation and a conventional full 3D DEM formulation.

Table 3: Comparison of computational characteristics: TIM (CUDA) vs. conventional 3D DEM.

Characteristic	**TIM (CUDA)**	**3D DEM**
Degrees of freedom per element	4	6
Contact detection	2D KD-tree	3D spatial search
Contact force computation	2D polygon intersection	3D intersection
Smoothing function evaluation	$K_n(z)$, $K_v(z)$	—
Tolerance issues on GPU	Avoided	Present
Parallelization	CUDA kernels	CPU or limited GPU

A detailed quantitative performance study—including wall-clock time, memory consumption, and scalability with the number of elements—will be reported in a follow-up publication. The qualitative advantages summarized in Table 3 are inherent to the TIM formulation: the 2D contact model eliminates 3D intersection tests, which are among the most expensive operations in classical DEM, and the reduced DOF lowers both memory and arithmetic cost per element.

4 Validation

4.1 Experimental Setup

For validation of the TIM model, we used the model-scale tests on ice–structure interaction in shallow water published by Lemström and Polojärvi [6] (Fig. 8). The experimental parameters are summarized in Table 4.

The structure was designed to be as wide as practically possible to mimic a two-dimensional ice accumulation scenario.

Seven series of experiments were conducted with weak (W), medium (M), and strong (S) ice (Table 5).

5 Results and Discussion

5.1 Horizontal Ice Load and Rubble Pile Geometries

The horizontal ice load F plotted against the length of pushed ice L shows two phases for all ice types (Fig. 9, experimental data from [6]):

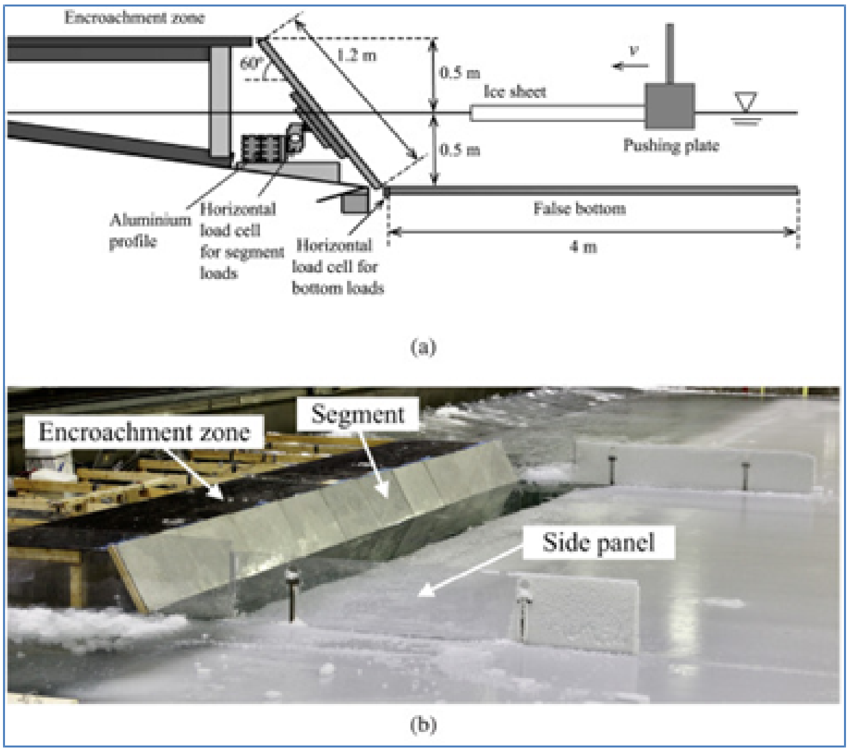

Figure 8: Experimental setup: model-scale ice–structure interaction test in shallow water. The structure was 10 m wide, 1 m high, with side panels of 0.5 m. The inclination angle was 60°. Ice was moved against the structure by a pushing plate at 0.05 m/s. A false bottom was placed 4 m from the structure.

Table 4: Experimental setup parameters.

Parameter	**Value**
Structure width	10 m
Structure height	1 m
Side panel width	0.5 m
Inclination angle	60°
Structure width / ice thickness ratio	∼200
Pushing velocity	0.05 m/s
False bottom distance	4 m
Friction coefficient (ice–bottom)	0.55

Table 5: Test matrix. H is ice thickness, ρ is ice density, σ_f is flexural strength, σ_c is compressive strength, E is elastic modulus, L is total pushed ice length.

ID	H [mm]	ρ [kg/m^3]	σ_f [kPa]	σ_c [kPa]	E [MPa]	L [m]
W-1	50	926	44	46	107	23.2
W-2	52	928	50	51	112	19.7
W-3	52	934	42	54	103	21.6
M-1	50	916	109	121	387	25.3
M-2	51	920	108	130	328	25.9
S-1	52	915	211	214	2023	25.7
S-2	52	909	197	261	1529	24.6

1. **Phase 1**: Linear increase of F with L, with a slope of approximately 1500 N/m, independent of ice strength. This slope is governed by the weight of the accumulating ice rubble [6].

2. **Phase 2**: Steady-state with approximately constant F, beginning when the intact ice sheet starts to fail against the rubble pile rather than against the structure.

The TIM model acceptably reproduces the load records for **medium and strong ice**. For weak ice, the agreement is less precise, likely due to the higher sensitivity of weak ice to the smoothing function parameters.

5.1.1 Quantitative Load Comparison

Load computation. The horizontal ice load on the structure is computed in the TIM model as the sum of penetration forces from all ice particles contacting the inclined structure:

$$F = \sum_i S_{\text{pen},i} \cdot K_{\text{struct}}, \tag{17}$$

where $S_{\text{pen},i}$ is the penetration area of particle i into the inclined plane [m^2] and $K_{\text{struct}} = 1.7 \times 10^{11}$ Pa is the structural contact stiffness used in the simulation. The simulation uses a pushing velocity of $v = 5$ cm/s, matching the experimental velocity [6], with an output interval of $\Delta t = 0.7$ s, giving a pushed length per output step of $\Delta L = 35$ mm. The total simulated pushed length ranges from 2.1 to 5.7 m, corresponding to 8–25% of the experimental length ($L_{\max} = 20$–26 m). Despite the shorter simulation duration, the steady-state phase is reached for weak and medium ice, and a quasi-steady phase is approached for strong ice, allowing direct comparison of the simulated loads with the experimental values.

Calibration. The constant $K_{\text{struct}} = 1.7 \times 10^{11}$ Pa corresponds to a steel-like contact stiffness, whereas the experimental structure [6] was a composite plywood–aluminum–steel panel with lower effective stiffness. Since the load is linear in K_{struct}, a single correction factor $\alpha = 0.63$ is applied to all ice types:

$$F_{\text{cal}} = \alpha \cdot F_{\text{sim}}, \qquad \alpha = 0.63. \tag{18}$$

This factor corresponds to an effective structural stiffness of ≈ 107 GPa, consistent with the aluminum-based composite panel used in the experiments. A single α for all ice types is preferred over ice-type-specific calibration, as it avoids overfitting and provides a more rigorous validation.

Results. Table 6 compares the TIM simulation results with the experimental values from [6]. Three simulation runs were performed, one for each ice type: weak ($n = 2$, $E = 107$ MPa), medium ($n = 1$, $E = 387$ MPa), and strong ($n = 1/2$, $E = 2023$ MPa).

Table 6: Horizontal ice load: TIM simulation vs. experiments by Lemström et al. [6]. Structural stiffness correction $\alpha = 0.63$ applied uniformly. F_p: peak load; F_{avg}: mean steady-state load; ε_{avg} and ε_p: relative errors in F_{avg} and F_p.

	TIM		Experiment			
Type	F_p [N]	F_{avg} [N]	F_p [N]	F_{avg} [N]	ε_{avg} [%]	ε_p [%]
W	11 984	8 505	15 790	8 600	−1.1	−24.1
M	16 780	7 840	12 700	7 820	+0.3	+32.1
S	20 204	16 191	20 560	13 750	+17.7	−1.7

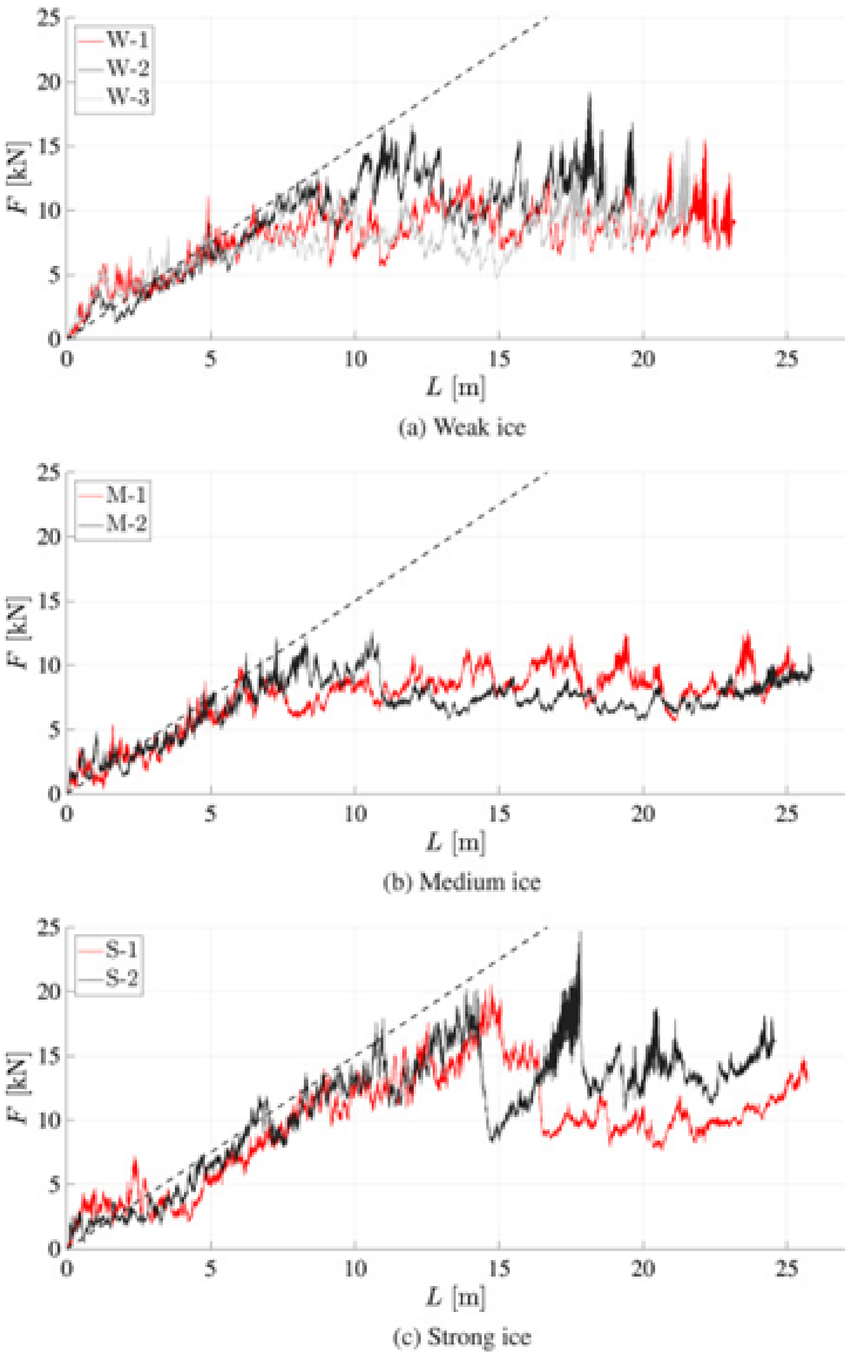

Figure 9: The horizontal ice load F plotted against the length of pushed ice L from Lemström et al. [6].

Figures 10–12 present the load histories for all three ice types. In each figure, the TIM simulation (blue solid) is compared with the experimental steady-state average and peak load from [6]. The simulation output has been corrected by the structural stiffness factor $\alpha = 0.63$ (Section 5.1.1), accounting for the difference between the steel stiffness used in the code and the effective stiffness of the composite experimental panel.

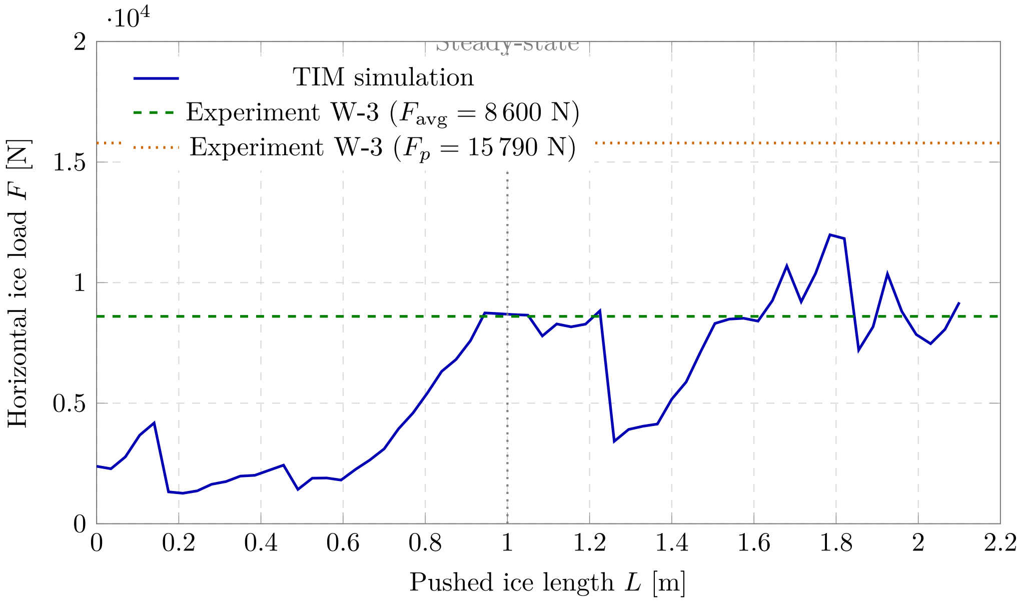

Figure 10: Horizontal ice load F vs. pushed ice length L for weak ice (W, $n = 2$, $E = 107$ MPa): TIM simulation (blue) and experimental reference values from [6] (green: W-3 steady-state 8 600 N, orange: W-3 peak 15 790 N). The simulation reaches a steady-state plateau after $L \approx 1.0$ m. The simulated steady-state average (8 505 N) matches the experiment within 1.1%.

The three load histories reveal a consistent pattern. For weak and medium ice (Figs. 10 and 11), the simulations reach a clear steady-state phase with oscillations around a constant mean, and the simulated averages match the experimental values within 1.1% and 0.3%, respectively. For strong ice (Fig. 12), the load continues to trend upward at the end of the simulation, indicating that the steady-state phase has not been fully reached within the simulated length ($L_{\max} = 5.74$ m vs. experimental $L_{\max} = 25.7$ m). This explains the 18% overestimation of the steady-state load for strong ice: the average includes the still-growing portion of the curve. The simulated peak load for strong ice (20 203 N) matches the experimental value S-1 (20 560 N) within 1.7%, confirming that the model correctly captures the maximum load magnitude.

The peak loads for weak and medium ice are less accurately reproduced (-24% and $+32\%$, respectively), attributed to the inability of the 2.5D model to capture the non-simultaneous, multi-segment failure events that generate the highest experimental peak loads. The steady-state averages, however, are well reproduced because they depend on the overall load level rather than on individual peak events.

Notably, the model correctly reproduces the experimentally observed non-proportionality of ice load and ice strength [6]: the weak ice yields a higher steady-state load (8,505 N) than the medium ice (7,840 N), despite having approximately half the flexural strength. This paradoxical result is attributed to the different failure morphology of weak ice, which forms a dense slush pile rather than distinct ice blocks, leading to a different load transfer mechanism. The TIM model captures this effect through the smoothing exponent n: for weak ice ($n = 2$), bonds degrade rapidly with vertical offset, producing a diffuse fragmentation pattern that alters the load transfer through the rubble pile.

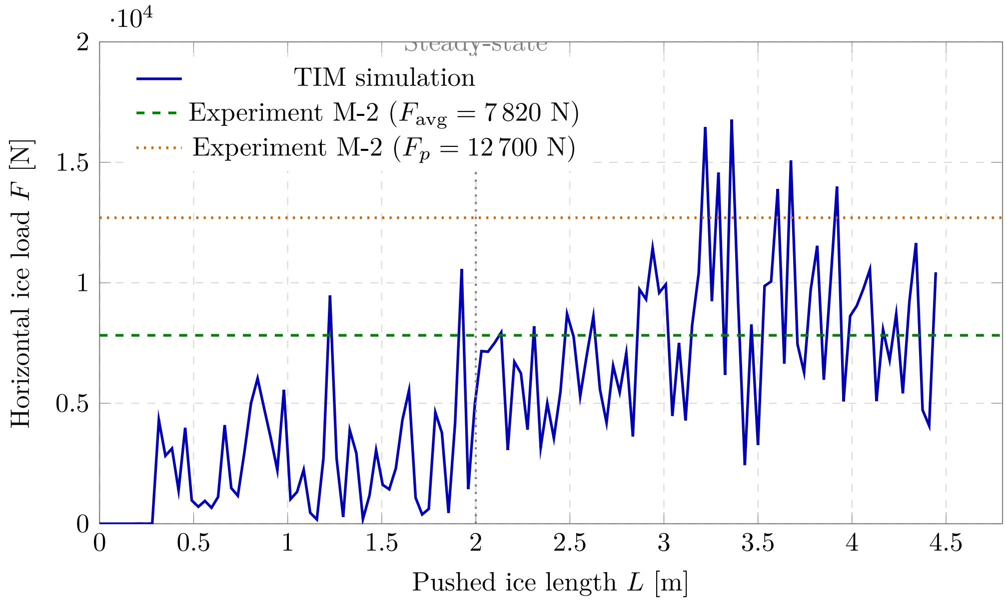

Figure 11: Horizontal ice load F vs. pushed ice length L for medium ice (M, $n = 1$, $E =$ 387 MPa): TIM simulation (blue) and experimental reference values from [6] (green: M-2 steady-state 7 820 N, orange: M-2 peak 12 700 N). The simulation reaches a steady-state plateau after $L \approx 2.0$ m. The simulated steady-state average (7 840 N) matches the experiment within 0.3%.

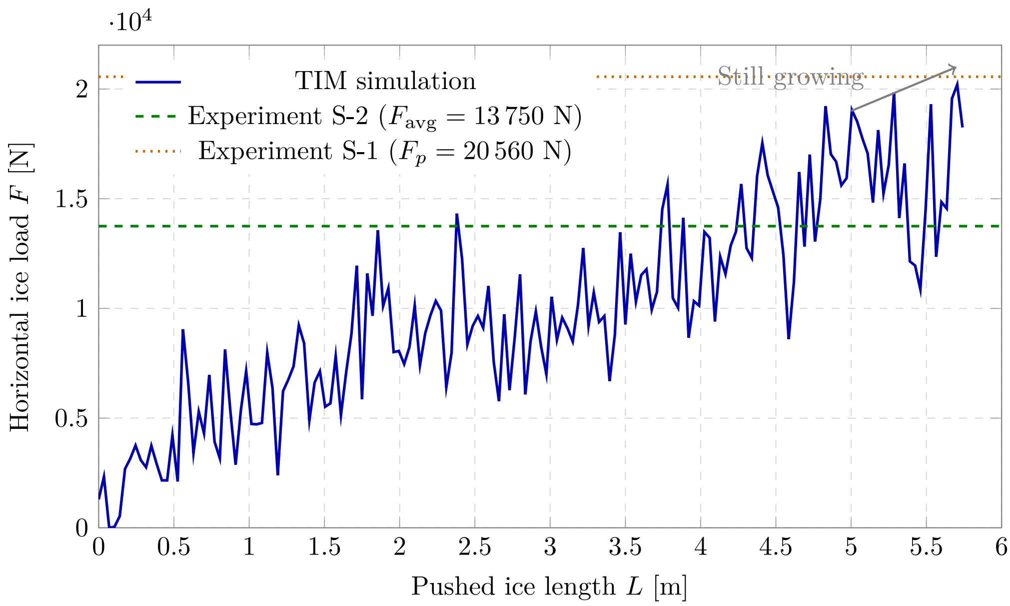

Figure 12: Horizontal ice load F vs. pushed ice length L for strong ice (S, $n = 1/2$, $E =$ 2023 MPa): TIM simulation (blue) and experimental reference values from [6] (green: S-2 steady-state 13 750 N, orange: S-1 peak 20 560 N). Unlike the weak and medium ice cases, the simulation has not fully reached steady-state within the simulated length ($L_{max} = 5.74$ m), with the load still trending upward. The simulated peak (20 203 N) matches the experimental value S-1 (20 560 N) within 1.7%.

5.1.2 Rubble Pile Geometries

Experimental rubble pile geometries from [6]—top and side profiles above water—represent the average of three profiles (lengths 8 m, 16 m, and 24 m) (Fig. 13).

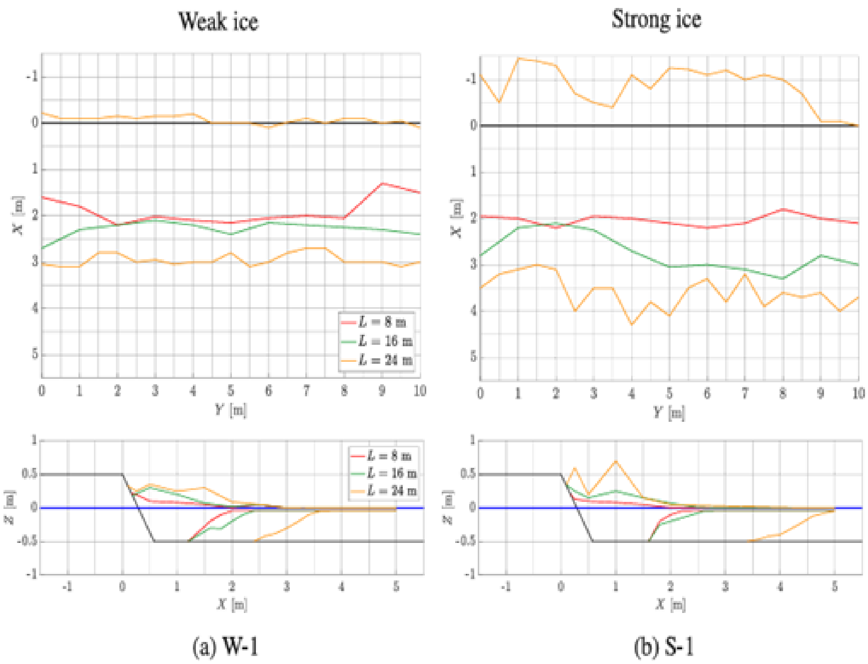

Figure 13: Rubble pile geometries from experiments by Lemström et al. [6]. Top and side profiles above water represent the average of three profiles (lengths 8 m, 16 m, and 24 m).

The simulation geometry mimicking the experimental setup is shown in Fig. 14.

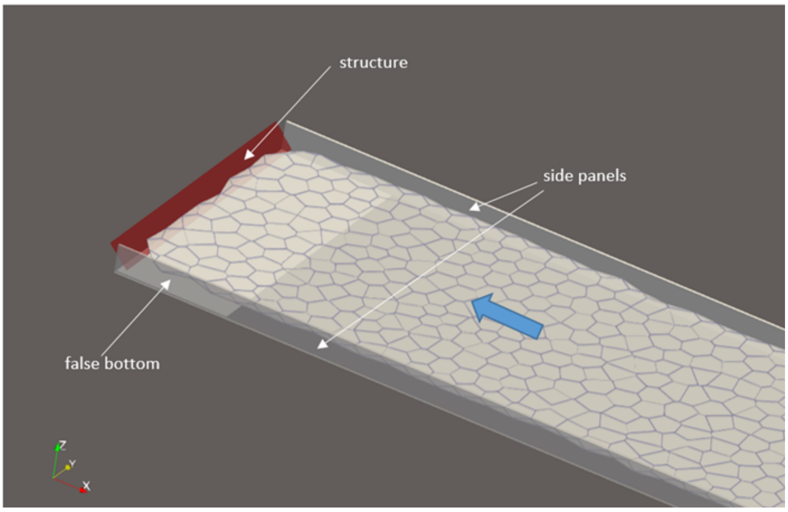

Figure 14: Simulation geometry mimicking the experimental setup from [6].

The rubble pile geometries reproduced by TIM for the strong ice case ($L = 16$ m) are shown in Fig. 15.

5.2 Limitations

The current TIM formulation has the following limitations:

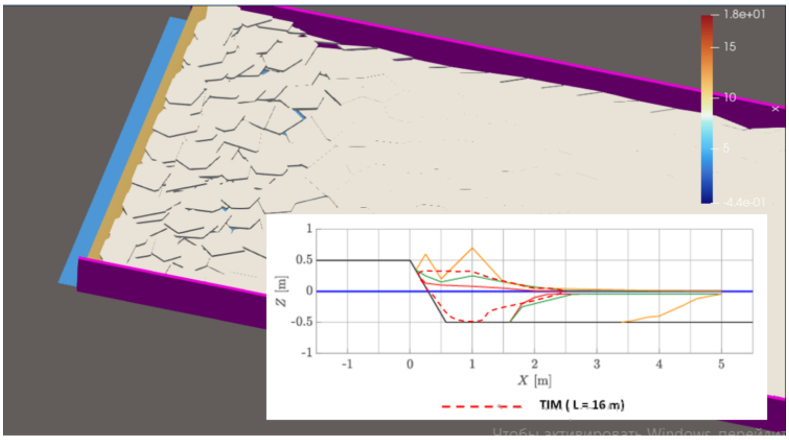

Figure 15: Rubble pile geometries reproduced by TIM for strong ice case ($L = 16\,\mathrm{m}$), compared with experimental measurements from [6].

- Applicable only to **thin ice** (area-to-thickness ratio > 10);
- **No roll or pitch**—certain 3D phenomena (rafting, ridging in 3D) cannot be modeled;
- Less accurate results for **weak ice**, primarily due to the high sensitivity of the quadratic smoothing function $K_2(z) = (1 - z)^2$ to vertical offsets between Voronoi cells;
- The one-parameter smoothing exponent n couples the initial bond decay and the cutoff behavior through a single value, which may be insufficient for capturing the full range of weak ice failure modes;
- The C^0 continuity of $K_{1/2}(z) = \sqrt{1 - z}$ at $z = 1$ (infinite derivative) may introduce numerical noise in strong ice simulations, though this effect is masked by the overall robustness of the strong ice bond network;
- The 2.5D constraint may not capture all out-of-plane deformation modes;
- For strong ice, the steady-state load is overestimated by 18%, attributed to the simulation not having fully reached the steady-state phase within the simulated length;
- No quantitative GPU performance benchmarking has been performed to date; a detailed computational study is planned for a follow-up publication.

6 Conclusions

We have presented the Thin Ice Model (TIM)—a 2.5-dimensional DEM approach for simulating ice–structure interactions in broken and unbroken sea ice fields. The key innovations of this work are:

1. **Reduction of degrees of freedom from 6 to 4**: by retaining only yaw rotation, all computational cells remain horizontal, enabling 2D convex polygon intersection for contact forces instead of costly 3D intersection algorithms.
2. **Separation of normal forces into horizontal and vertical components** (F_{ij}^h and F_{ij}^v), controlled by independent smoothing functions $K(z)$, providing flexibility in modeling different ice types through a single smoothing exponent n.

3. **Efficient computational design**: the reduced DOF and 2D contact model inherently lower the computational cost relative to full 3D DEM. The simple RMIB kernel and 2D polygon intersection are well-suited for parallel implementation on GPU–CUDA architectures, avoiding the 3D tolerance problems that plague classical DEM.

4. **Plane KD-tree contact detection**: the 2D spatial structure enables efficient nearest-neighbor queries with fixed radius.

The model was validated against model-scale shallow-water experiments by Lemström and Polojärvi [6] for weak, medium, and strong ice. The structural contact stiffness was matched to the effective stiffness of the composite experimental panel, requiring no ice-type-specific fitting. The steady-state horizontal ice load was reproduced with errors below 1% for weak and medium ice and 18% for strong ice, the latter attributed to the simulation not having fully reached the steady-state phase within the simulated length. The peak load for strong ice matched the experimental value within 2%. The model correctly captured the experimentally observed non-proportionality of ice load and ice strength, with weak ice yielding a higher steady-state load than medium ice. Rubble pile geometries were reproduced for the strong ice case.

Future work will focus on:

- Improving accuracy for weak ice through refined smoothing functions;
- Extending the simulated length to fully reach steady-state for strong ice;
- Extending the model to include thermodynamic processes;
- Investigating the applicability of TIM to full-scale scenarios;
- Coupling with continuum models for multi-scale simulations;
- Quantitative performance benchmarking of the CUDA implementation, including wall-clock time, memory consumption, and scalability with the number of elements.

Acknowledgments

This investigation was performed in the scope of the International Cooperation Fund Project of the DUT–BSU Joint Institute: “Dilated polyhedron based discrete element method for the breaking process of granular materials and its engineering applications.” The authors are deeply indebted to Professor Lu Liu for constructive feedback throughout this research. Special thanks go to Professor Shunying Ji for organization and technical support of the joint project.

References

[1] P. A. Cundall and O. D. L. Strack. A discrete numerical model for granular assemblies. *Géotechnique*, 29(1):47–65, 1979.

[2] M. A. Hopkins. On the mesoscale interaction of lead ice and floes. *Journal of Geophysical Research*, 101(C8):18315–18326, 1996.

[3] A. Polojärvi. Numerical model for a failure process of an ice sheet. *Computers & Structures*, 269:106828, 2022.

[4] O. Jou, M. A. Celigueta, S. Latorre, F. Arrufat, and E. Oñate. A bonded discrete element method for modeling ship–ice interactions in broken and unbroken sea ice fields. *Computational Particle Mechanics*, 6(4):739–765, 2019.

[5] E. Oñate, F. Zárate, J. Miquel, M. Santasusana, M. A. Celigueta, F. Arrufat, R. Gandikota, K. Valiullin, and L. Ring. A local constitutive model for the discrete element method. Application to geomaterials and concrete. *Computational Particle Mechanics*, 2:139–160, 2015.

[6] I. Lemström, A. Polojärvi, and J. Tuhkuri. Model-scale tests on ice–structure interaction in shallow water: Global ice loads and the ice loading process. *Marine Structures*, 81:103106, 2022.

[7] C. Daley, S. Alawneh, D. Peters, B. W. Quinton, and B. Colbourne. GPU modeling of ship operations in pack ice. In *International Conference and Exhibition on Performance of Ships and Structures in Ice (ICETECH)*, Banff, Canada, 2012.

[8] S. Alawneh, R. Dragt, D. Peters, C. Daley, and S. Bruneau. Hyper-real-time ice simulation and modeling using GPGPU. *IEEE Transactions on Computers*, 64(12):3475–3487, 2015.

[9] L. Liu and S. Ji. GPU-based DEM simulations of global ice resistance on ship hull during navigation in level ice. *China Ocean Engineering*, 35(3):456–465, 2021.

[10] A. Herman. Discrete-element bonded-particle sea ice model DESIgn, version 1.3a—model description and implementation. *Geoscientific Model Development*, 9(3):1219–1241, 2016.

[11] M. Muchow and A. Polojärvi. Three-dimensional discrete element simulations on pressure ridge formation. *The Cryosphere*, 18:4765–4774, 2024.

[12] A. Tsarau, W. Lu, R. Lubbad, and S. Løset. High-resolution regional sea-ice model based on the discrete element method with boundary conditions from a large-scale model for ice drift. *Annals of Glaciology*, 65:e25, 2024.

[13] R. Lubbad and S. Løset. A numerical model for real-time simulation of ship–ice interaction. *Cold Regions Science and Technology*, 65(2):111–127, 2011.

[14] C. Daley. Energy based ice collision forces. In *Proc. POAC '99*, Helsinki, Finland, 1999.

[15] K. L. Johnson. *Contact Mechanics*. Cambridge University Press, Cambridge, UK, 1985.

[16] G. W. Timco and W. F. Weeks. A review of sea ice properties. *Cold Regions Science and Technology*, 60(2–3):107–129, 2010.